

Deciphering, Designing, and Realizing Self-Folding Biomimetic Microstructures Using a Mass-Spring Model and Inkjet-Printed, Self-Folding Hydrogels

Chunxiao Cui, Jie Yin, and Li-Hsin Han*

Flat, organic microstructures that can self-fold into 3D microstructures are promising for tissue regeneration, for being capable of distributing living cells in 3D while forming highly complex, biomimetic architectures to assist cells in performing regeneration. However, the design of self-folding microstructures is difficult due to a lack of understanding of the underlying formation mechanisms. This study helps bridge this gap by deciphering the dynamics of the self-folding using a mass-spring model. This numerical study reveals that self-folding procedure is multi-modal, which can become random and unpredictable by involving the interplays between internal stresses, external stimulation, imperfection, and self-hindrance of the folding body. To verify the numerical results, bilayered, hydrogel-based micropatterns capable of self-folding are fabricated using inkjet-printing and tested. The experimental and numerical results are consistent with each other. The above knowledge is applied to designing and fabricating self-folding microstructures for tissue-engineering, which successfully creates 3D, cell-scaled, and biomimetic microstructures, such as microtubes, branched microtubes, and hollow spheres. Embedded in self-folded microtubes, human mesenchymal stem cells proliferate and form linear cell-organization mimicking the cell morphology in muscles and tendons. The above knowledge and study platforms can greatly contribute to the research on self-folding microstructures and applications to tissue regeneration.

human tissues that were permanently damaged due to trauma or diseases. It has been found that microstructures with 3D shapes, biochemical properties, and mechanical properties that closely mimic the extracellular microenvironments in the human body are crucial towards successful tissue regeneration.^[2] In the native tissues, the extracellular matrix (ECM) consists of various proteins and polysaccharides that form a complex network of pores, channels, and irregular cavities (Figure 1). Within these structures are living cells that perform bioactivities to maintain the tissue's function.^[3] Organic microstructures that resemble such ECM may promote cell proliferation, cell-cell organization, migration, and gene-expression that lead to the regeneration of desired tissues.^[2a,4]

Despite the great potentials, fabrication of 3D microstructures for tissue-engineering applications remains challenging. Conventional microfabrication methods, such as photolithography, are suitable for assembling metals and metallic oxides into 2D microstructures but are suboptimal for processing organic compounds

constructing 3D ECM mimicking microstructures.^[5] Additive manufacturing, such as 3D printing and stereolithography,^[1c-f] is capable of creating 3D organic structures. Some of these methods, such as digital micromirror device (DMD) stereolithography and two-photon stereolithography,^[6] can fabricate 3D scaffolds with subcellular size feature down to a micrometer to sub-micrometer scale. However, the need to uniformly populate 3D scaffolds with living cells presents a major challenge to additive manufacturing methods. To incorporate living cells, scaffolds fabricated by the above methods will be treated with cell infiltration, in which cells are seeded from outside the scaffolds and are left to diffuse or migrate into the microstructures. However, the cell-scale, small features in the fabricated scaffold could easily hinder the diffusion and migration of cells,^[1a,7] preventing the cells from reaching the inner parts of a 3D scaffold consisting of the microstructures (Figure 1B,D). This difficulty in cell distribution can lead to acellular zones in a scaffold, making it difficult to repair a sizable body defect at the length scale of organs or limbs.^[8] 3D bioprinting may circumvent this problem by mixing cells with the printing

1. Introduction

Recent emerging fields in the healthcare industry, particularly the Regenerative Medicine, have shown the growing needs of microstructures that are made of organic compounds and at the length-scale of biological cells (1–100 μm).^[1] These microstructures are being developed as implants aiming at regenerating

C. Cui, Prof. L.-H. Han
Department of Mechanical Engineering and Mechanics
Drexel University
3141 Chestnut St., Philadelphia, PA 19104, USA
E-mail: lh573@drexel.edu

Prof. J. Yin
Department of Mechanical and Aerospace Engineering
North Carolina State University
Raleigh, NC 27695, USA

 The ORCID identification number(s) for the author(s) of this article can be found under <https://doi.org/10.1002/adfm.202003959>.

DOI: 10.1002/adfm.202003959

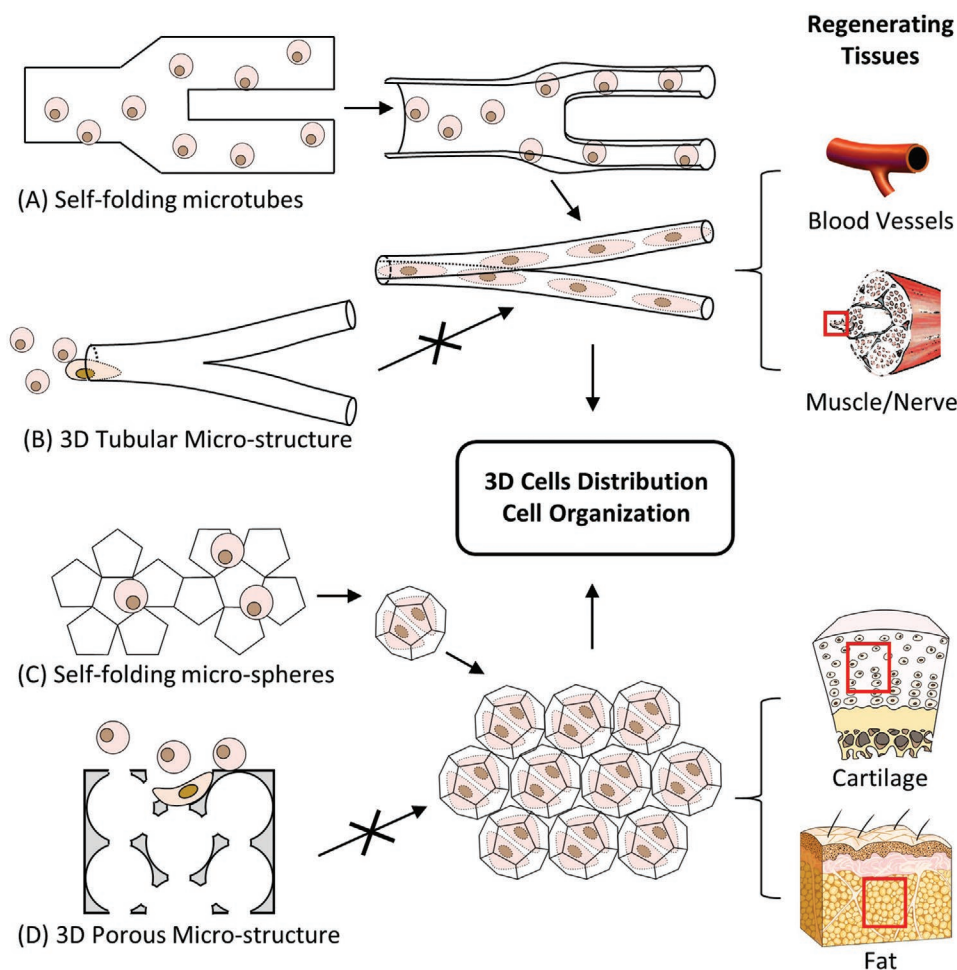


Figure 1. A,C) Self-folding method enables uniform cell-delivering in 3D and facilitates cell–cell organization formation, which may lead to functional tissues. B,D) In contrast, scaffolds of prefabricated, cell-size 3D microstructures, such as micropores and channels, can obstruct cell delivery.

biomaterial.^[9] However, despite being uniformly distributed, the cells printed with the biomaterial can be confined within a tight space formed by the biomaterial. In such a case, it can become difficult for the cells to spread, migrate, form cell–cell organization, or produce ECM.^[10]

Emerged in recent years, self-folding of 3D microstructures from 2D flat micropatterns^[11] provides a promising way for overcoming the aforementioned challenges in regenerative medicine. Through folding, rolling, or wrinkling, these flat microstructures can transform into 3D, biomimetic microstructures, including tubular, spherical, or more complex 3D shapes that resemble the architectures of ECM^[12] (Figure 1). To enable a 2D microstructure to self-fold, the most common method is by assembling a microstructure with layers of different polymers that perform distinct levels of volume expansion (or contraction) in response to environmental stimuli,^[11b,13] such as pH value, temperature, or the presence of specific chemicals.^[12a,b,14] This mismatched volume change produces internal stresses across the layers, which bends the microstructure and induces self-folding.

Self-folding microstructures provide the following advantages for tissue-engineering applications. First, it enables a uniform, 3D cell-distribution, as the user can distribute and culture cells

uniformly atop the unfolded microstructures, and then activate the self-folding leading to a cell-embedded 3D scaffold (Figure 1A,C). Second, 3D scaffolds of complex, biomimetic shape become much easier to produce. For example, to engineer a microvessel that is very thin and long in comparison with the typical size of cells, the user can culture blood vessel cells onto a flat, long and bilayered microrectangles that self-fold into a microscopic tube mimicking the microvessels (Figure 1A,B). Third, from the perspective of ease-to-use, flat and self-folding microstructures can be easily adapted by a physician or biologist that is familiar with the standard techniques for culturing cells in 2D, such as on a Petri-dish or multi-well plate, which helps accelerate the clinical application of regenerative medicine.

Accurate prediction of 2D to 3D shape transformation is essential to the self-folding micropatterns' designing, which determines the shapes of the resulting 3D microstructure. In previous studies, the design of the self-folding body is often based on a bilayered cantilever beam model^[15] to predict the static equilibrium curvature after folding. The simple model assumes a symmetric and unidirectional folding of the bilayered structure. However, self-folding is rather a complicated dynamic process and sensitive to the external perturbation, thus it could exhibit

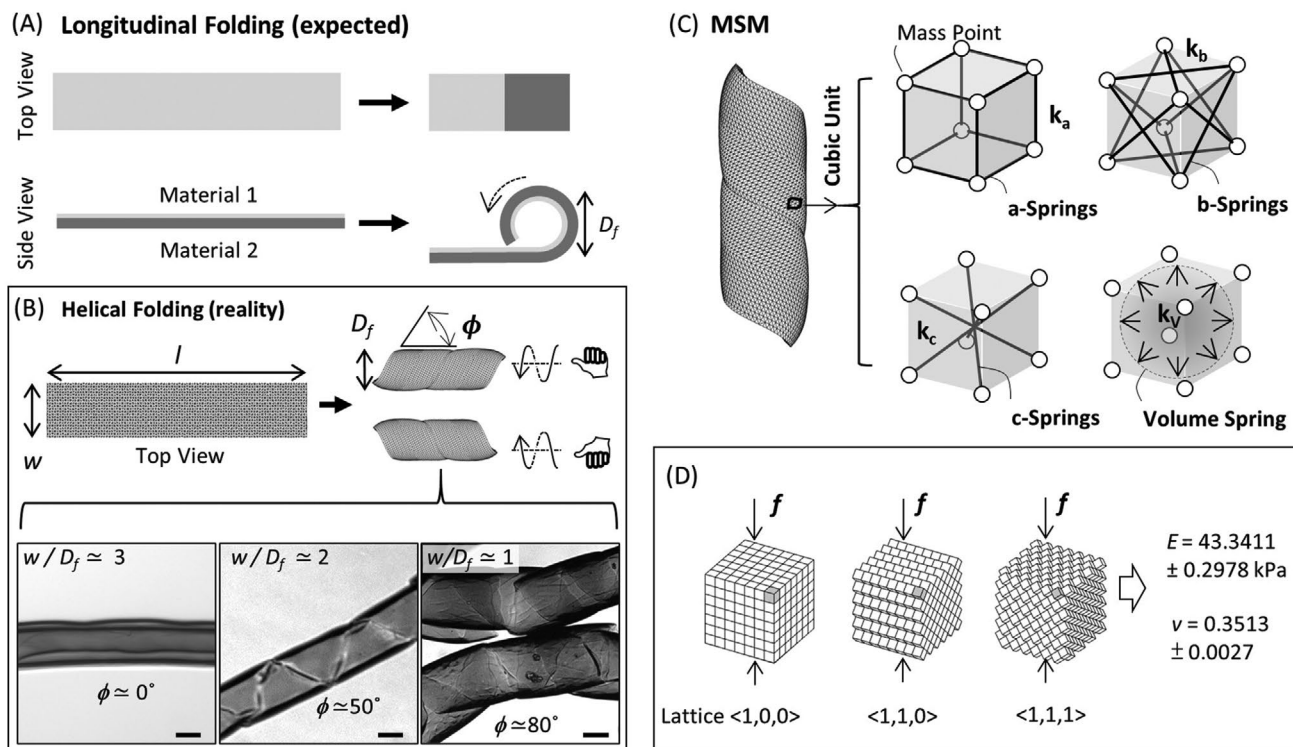


Figure 2. A) Based on the simple cantilever beam model (Equation (1)), a flat and bilayered microrectangle consisting of two layers of different expansion rates is expected to fold longitudinally and become a short tube. B) In reality, self-folding of bilayered microrectangles is more complex. B, lower left) The rectangles mostly transform into long tubes or B, lower middle and right) helical tubes. B, top right) The folding results of helical tubes are bi-modal, in which the twisting can be either left-handed or right-handed. C) These phenomena were repeatedly observed in our study. Scale Bars: all 100 μm . In this mass-spring method (MSM), a deforming body was simulated by a finite number of mass-points, which formed cubic units. Neighboring mass-points were coupled by virtual springs of spring constant k_a , k_b , or k_c , to simulate elasticity. Each virtual spring was coupled with a virtual damper of damping ratio ζ (not shown), which simulated internal frictions. Each cubic unit was also assigned with a volume spring k_v that resisted a change to the cubic unit's volume, which simulated Poisson's effect. D) The spring-constants were properly assigned to maximize the accuracy of MSM model.

asymmetric folding, intermediate folding, and rich multi-modal shape transition resulting in distinct self-folded shapes even from the same preset 2D micropatterns, as demonstrated in our studies (Figure 2) as well as from other groups.^[16] Such discrepancy and rich self-folding phenomena are far beyond the simple classical bilayer folding model. In addition, the underlying mechanism for rich dynamic shapes remains unclear^[16] and largely unexplored. Furthermore, we anticipate the self-folding from more complex micropatterns and 2D geometry to be more random and difficult to predict. Thus, a fundamental understanding of the self-folding dynamics is highly demanded to shed important light to guide the formation of shape-transforming microstructures, as well as to their biomedical applications.

In this study, to bridge the above knowledge gaps, we developed a numerical model to understand the complicated dynamics of self-folding of a 2D bilayered body that undergoes a heterogeneous volume expansion. We conducted experiments to validate the modeling results and later applied the results to designing self-folding tissue-engineering scaffolds. The numerical model was a mass-spring model (MSM) that allowed simulating, in real-time, the release of strain energy, the change of internal stresses, and the subsequent deformation of the 3D body. The modeling results revealed that the transition from the initial 2D micropattern to the final 3D shape can involve

multiple intermediate, distinct phases, which are found to be unstable and prone to being disrupted by stimuli from external forces. The modeling also indicated that, for 2D micropatterns with certain shapes, the shape-transformation is multi-modal and has more than one possible way to release strain energy, such that the same micropatterns may transform into different 3D microstructures. These simulation results were verified by physical models, in which two different biopolymers of distinct swelling rates were inkjet-printed into bilayered micropatterns that performed self-folding in water. Finally, the knowledge learned from the modeling was applied to fabricating self-folding micropatterns that transformed into biomimetic 3D shapes that resemble various types of tissues in human body.

2. Discrepancy with Classical Bilayer Folding Model

The bending of classical bi-strip model assumes a thin and long rectangle cantilever consisting of two layers of materials, which perform distinct rates of volume expansion or contraction (Figure 2A). Under mismatched deformation between the two layers, it self-folds into a bended structure with its virtual diameter D_f given by^[15]

$$D_f = 2h' \frac{3 \left(1 + \frac{h_1(1+\alpha_1)}{h_2(1+\alpha_2)} \right)^2 + \left(1 + \frac{E_1 h_1(1+\alpha_1)}{E_2 h_2(1+\alpha_2)} \right) \cdot \left(\frac{h_1(1+\alpha_1)}{h_2(1+\alpha_2)} \right)^2 + \frac{E_2 h_2(1+\alpha_2)}{E_1 h_1(1+\alpha_1)}}{6(\alpha_2 - \alpha_1) \left(1 + \frac{h_1(1+\alpha_1)}{h_2(1+\alpha_2)} \right)^2} \quad (1)$$

where h' is the total thickness of the bilayered film after expansion/contraction ($h' = h_1(1 + \alpha_1) + h_2(1 + \alpha_2)$), h_1 and h_2 are the initial thicknesses of the two layers, α_1 and α_2 are the expansion rates of the two layers (negative for contraction), and E_1 and E_2 are the Young's moduli of the two layers after expansion/contraction. The above model assumes that the folding of the bilayered rectangle is always symmetric, unidirectional, and in the longitudinal direction, as illustrated in Figure 2A.

The thickness of the micropattern h' and the thickness ratio between the top and bottom layer h_1/h_2 determine the folding diameter. However, our previous studies showed that micropatterns of the same printed thickness, which gave the same folding diameter, can perform dramatically different self-folding. This inconsistency between the experiments and the classical bilayer folding model has been repeatedly observed in this work (e.g., Figure 2B). Figure 2B shows that two polymers of different swelling rates in water were assembled into bilayered microrectangles which self-folded into microtubes in the presence of water. The width, length, and layer thickness of the microrectangles were changed to tune the diameter of the microtubes. The folding diameters (D_f) of the microtubes roughly matched the estimation of Equation (1). However, instead of folding in the longitudinal direction and becoming a short tube (as Figure 2A and Equation (1) assumes), the microrectangles self-folded into either a straight long tube (Figure 2B, lower-left) or a helical tube (Figure 2B, lower-middle and lower-right), depending on the micropattern dimensions (length, width, and layer thickness). Moreover, the self-folding results of microrectangles (straight tubes or helical tubes) and the helix angles (ϕ) of the helical tubes were found to be correlated with the ratios between the width, length, and folding diameter of the microtube (Figure 2B, bottom). Most interestingly, the folded helical tubes exhibited both left-hand and right-hand chirality (Figure 2B). This bi-modal folding indicates that the release of strain-energy during the self-folding of microrectangles has more than one possible route, which causes unpredictable self-twisting direction. Asymmetric folding of rectangular structures as such has been reported elsewhere, but the underlying mechanism remains largely unclear.^[16] For micropatterns that are more complex than the microrectangles, we anticipate the final shape of self-folding to be more random and difficult to predict. To reveal the underlying mechanism, next, we will use a mass-spring model to understand the self-folding dynamics of shape-transforming microstructures and compare with further experiments as discussed later.

3. MSM to Study the Dynamics of 2D to 3D Shape Transformation

3.1. Deciphering the Dynamics of Self-Folding Using MSM

To simulate a complex deformation such as the self-folding of multilayered micropatterns, one may use either a continuum

mechanics based algorithm, such as finite element method (FEM),^[17] or a lump-mass algorithm, such as MSM.^[18] The former is a continuum model based on rigorous constitutive equations.^[19] In contrast, a lump-mass algorithm such as MSM approximates a continuum body by a finite number of mass-points that are connected by virtual springs. An MSM-based lump-mass algorithm was selected for this study for the following reasons.

A continuum mechanics algorithm can accurately predict the shape transformation of a wide range of materials, from metals to complex living tissues. However, such modeling demands a rigorous description of the boundary conditions that is often incompatible with arbitrary and unpredicted events. In addition, it remains challenging to converging under sophisticated multi-body contact and fluid-structures interactions, such as the collision between folding bodies and drag resistance force from water during folding in solution. For folding deformation, a continuum mechanics algorithm also requires the users to model the body by a large deformation context that demands extensive computation efforts, such as the total Lagrangian explicit dynamic (TLED) algorithm for FEM.^[20] These issues render the continuum mechanics algorithm time-consuming and inefficient for simulating a 2D to 3D shape transformation involving contacts and fluid-soft-structure interactions during folding.

In contrast, in a lump-mass model such as the MSM algorithm, a deforming body is approximated by concentrated mass-points that are connected by virtual springs. The spring-constants are assigned to provide internal stresses between the mass-points in response to deformation, simulating the elasticity of the body.^[18a] External forces from collisions, frictions, and drags are applied directly to the mass-points. The shape transformation of the 2D body is calculated simply by applying Newton's second Law, i.e., $F = MA$, to the mass-points, generating motions of the mass-points and subsequently the shape transformation of the deforming body. In comparison with continuum models, the lump-mass model has the advantages of being highly flexible, easy to use, and efficient in simulating large deformation.

3.1.1. Modeling Young's Modulus, Internal Damping, and Poisson's Ratio

Our MSM model was based on established algorithms^[18a,b,21] and implemented in MATLAB (version 2019a). Details of modeling are provided in Section S1.1 in the Supporting Information. In this model, a 2D body undergoing self-folding was simulated by a number of cubic units (Figure 2C,D). Each vertex of the cubic units was assigned with a mass-point with its mass determined by the material's density.

Adjacent mass-points were coupled by virtual springs, which determined the body's Young's modulus. The virtual

springs between the nearest neighbor mass-points had spring constant of k_a , and the ones between the second and third nearest neighbor mass-points had spring constants of k_b and k_c , respectively (Figure 2C, a, b, c-Springs). The values of k_a , k_b , and k_c (unit: N m^{-1}) were regulated by the following relations: $k_a = \alpha + \beta$, $k_b = \alpha$, and $k_c = 3/8 \beta$, with the values of α and β being selected to obtain the desired Young's modulus. In simulating an isotropic object, former studies^[18a,b,21] established that the above confinements to k_a , k_b , and k_c maximize the accuracy of the MSM algorithm in comparison with continuum models.

Internal friction is a key element in the modeling of polymeric materials such as hydrogel. To simulate the effects of internal frictions, each virtual spring was assigned with a virtual damper of damping-ratio ζ that was between 0 and 1. This value determined whether the body would oscillate during self-folding, with $\zeta = 0$ allowing nonstop oscillation and $\zeta = 1$ eliminating oscillation.^[22]

Poisson's ratio determines the ability of a body to resist a change to the volume.^[23] To simulate the Poisson's effect and create a tunable Poisson's ratio,^[18c] in addition to the virtual springs, each cubic unit was introduced with an isotropic spring that resists a change of the unit's volume by a spring constant k_v (Figure 2C, Volume Spring). In each unit, the difference between the unit's current volume v_u and the unit's equilibrium volume $v_{u\text{-equi}}$ (at which all linear springs in the unit are relaxed) was calculated ($\Delta v_u = v_u - v_{u\text{-equi}}$). This value was converted into an isotropic force $k_v \Delta v_u$, from the isotropic volume spring, between the cubic unit's mass center and the unit's mass-points. The direction of the isotropic force, i.e., contracting or expanding, was determined by the sign of Δv_u —contracting if $\Delta v_u > 0$ and expanding if $\Delta v_u < 0$. The constant k_v determines the magnitude of the isotropic force and thus the simulated body's Poisson's ratio. For example, when simulating a cubic block as shown in Figure 2D, increasing the value of k_v from 0 to 0.3 increased the Poisson's ratio from ≈ 0.25 to 0.35.

3.1.2. Approaching Mechanical Isotropy

Before using the MSM for simulation, we first examined whether the model is capable of approaching a mechanically isotropic object as the results from former studies showed.^[18a,b,21] To do so, a cubic body was created by assembling the cubic units according to three different lattice systems defined as $\langle 1,0,0 \rangle$, $\langle 1,1,0 \rangle$, and $\langle 1,1,1 \rangle$, as illustrated in Figure 2D. Simulated normal forces were applied uniformly in the z -axis direction, to the top and bottom surface of the cubic bodies, which caused the cubic bodies to extend longitudinally, while shortening laterally following Poisson's effect. The Young's modulus (E) and Poisson's ratio (ν) of the cubic body were calculated following standard mechanics formula.^[24] The results showed that the accuracy of the MSM algorithm was sufficient for yielding E and ν values across the three lattice directions with less than 0.8% error. For example, when using $k_v = 0.3$, $\alpha = 1 \times 10^{-6} \text{ N m}^{-1}$ and $\beta = 1 \times 10^{-6} \text{ N m}^{-1}$ (for spring constant k_a , k_b , and k_c), the modeling yielded $E = 43.3411 \pm 0.2978 \text{ kPa}$ and $\nu = 0.3513 \pm 0.0027$, with less than 0.8% variation across the three different lattice systems.

3.1.3. Self-Folding of Microrectangle is a Two-Phase Procedure

The MSM model was first applied to simulate the self-folding of a simple, bilayered microrectangle (Figure 3). The mechanical properties of the simulated microrectangles followed the data from the experiments ($E \approx 40 \text{ kPa}$ and $\nu \approx 0.35$). A bilayered rectangle of $125 \mu\text{m}$ in width and $500 \mu\text{m}$ in length was constructed by cubic units of $5 \times 5 \times 5 \mu\text{m}$ size. In our experiments, the total thickness of each layer increase by the number of stacking of microdroplets. Each microdroplet increased the thickness of the micropattern by about $1.3 \mu\text{m}$, as measured by a confocal microscope (data not shown). The MSM model was developed accordingly. For example, for the self-folding rectangles in Figure 5A, each layer was printed by four stacks of microdroplets, leading to layers of roughly $5 \mu\text{m}$ in thickness. In simulating the self-folding of such a microrectangle, therefore, the thickness of each simulated layer was set to $5 \mu\text{m}$. The lower layer of the rectangle was set for 59% swelling by length, and the top layer for 34% swelling by length. The damping ratio between mass-points (ζ) was tuned between 0.1 and 0.9 (in which range the model is allowed to oscillate) to examine the effect of ζ value on shape transformation.

In our experiment, the inkjet-printed micropattern was often incubated in an aqueous environment for several days before self-folding was activated. During the incubation, the micropattern was kept flat by a binding layer, which was coated on the substrate to retain the micropattern, so that living cells could have enough time to settle and spread on the micropattern. The binding layer was dissolved at a desired moment to activate self-folding, using a method that will be explained in a later section. Due to the accumulation of swelling stress, upon being released, the micropattern rapidly self-folded into a 3D structure (Video S1, Supporting Information). To model such preaccumulation of swelling stress and sudden release, in our MSM model the equilibrium length of the linear springs, l_{equi} , was increased for each cubic unit, by 59% for the lower layer and 34% for the upper layer, during a narrow period at the beginning of the simulation ($<1\%$ of total simulation time). This caused the springs to push apart the mass-points and the bilayered rectangle to deform. Besides the internal forces, resistant forces from the surrounding fluid (water), which decelerates self-folding, were applied to the mass-points at the surface of the bilayered rectangle according to the velocity of the mass-points, following the classical fluid mechanics formula for drag forces.^[25]

The simulations revealed that the self-folding of the microrectangles is a two-phase procedure consisting of a primary folding and a secondary folding. In the primary folding, strain energy from swelling caused the microrectangle to perform a dual-curvature deformation, in which the rectangle folded simultaneously along both the lateral and the longitudinal direction. As the folding continued, the lateral folding gradually dominated and the rectangle transformed into a half-tube that was long and axially symmetric, with roughly $110 \mu\text{m}$ D_f and $360 \mu\text{m}$ folding circumference ($C_f = \pi \times D_f$). At this point, the rectangle reached an equilibrium and the deformation ceased (Figure 3A, labeled by "*", also see Video S2 in the Supporting Information (0–7 s) for the folding process). To test whether this equilibrium was stable, an external disturbance (a simulated impulse of 10 ms duration) was applied to an arbitrary mass-point

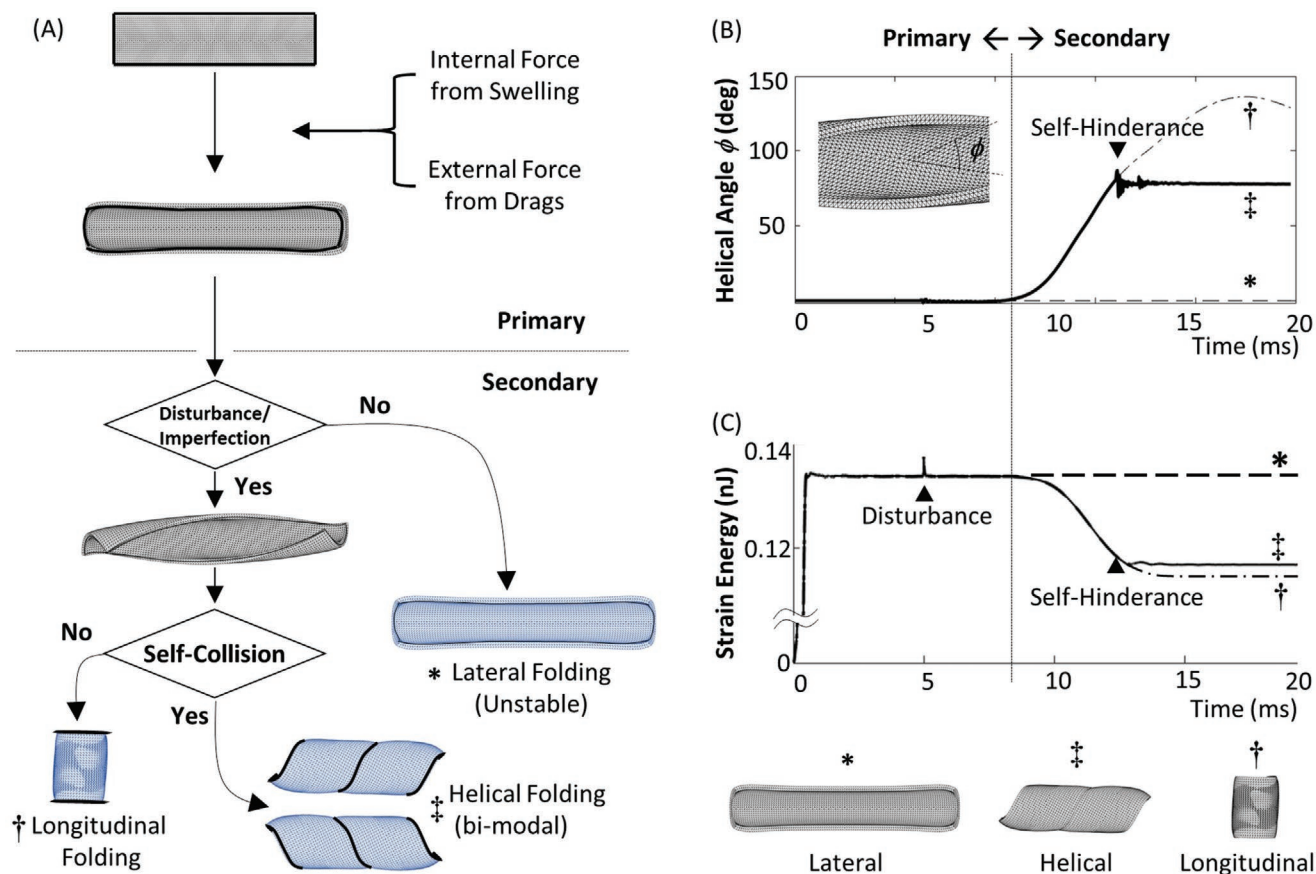


Figure 3. A) MSM modeling of a bilayered microrectangle. The modeling results revealed that the self-folding includes two phases: primary folding and secondary folding. In the primary folding, the bilayered microrectangle self-folds by the lateral direction and remains symmetric (“*”). The secondary folding is activated by either a disturbance or an introduction of imperfection to the model (“†” and “‡”). In the secondary folding, in the presence of self-hindrance, the microrectangle transforms into a helical tube, by either the left-handed or right-handed direction (“‡”). Whereas, in the absence of self-hindrance, the helical tube continues to twist until becoming a short tube (“†”). B, C) The changes of helical angle and strain energy throughout the modeling. Shortly after the primary folding, a small disturbance was introduced to the model for both “†” and “‡.” Self-hindrance is enabled on “‡” only. B, “†”) Self-twisting of microrectangle transforms the lateral folding (primary folding) to a longitudinal folding (secondary folding), in which the twist angle ϕ increases from 0° toward 90°. C, “†” and “‡” vs “*”). C, “‡”) The self-twisting releases more strain energy from the folding microrectangle. Self-hindrance interrupts the self-twisting and leads to a helical tube.

(Video 2, Supporting Information). The impulse was applied between the seventh and eighth seconds in the video. Interestingly, the impulse broke the equilibrium and triggered a secondary phase of folding, in which the half-tube began to twist and transformed into a helical tube, while maintaining the same D_f and C_f (Figure 3A, labeled by “‡,” also in Video S2 in the Supporting Information after eighth second). More importantly, this secondary folding was found to be bi-modal, in which the direction of twisting (right-handed or left-handed) could be changed by altering either the direction of the impulse or the mass-point to receive the impulse (Figure 3A, labeled by “†”). Other than external disturbance, a model’s internal imperfection, which makes the model not perfectly symmetric or uniform, can also lead to secondary folding. When imperfection was introduced, such as randomizing the spring constants, masses, or the mass-points’ positions by 0.1%, the transition between the primary and secondary folding became automatic, taking place without a disturbance (Video S3, Supporting Information). Besides, we found that changing damping ratio ζ

between 0.1 and 0.9 had negligible effects on the above results. For simplicity, we used $\zeta = 0.5$ for the following simulations.

3.1.4. Longitudinal Folding is Energetically Preferred

To understand how the strain energy evolves in self-folding, in this batch of simulation, we omitted the collision between mass-points and allowed the simulated body to overlap with itself, which means that we disabled the self-hindrance. In such a case, the twisting of half-tube continued until the helical structure transformed into a short tube (Figure 3A, labeled by “†,” also in Video S4, Supporting Information). Tracking on the strain energy of virtual springs showed that self-folding into a short tube (Figure 3C, labeled by “†”) leads to significantly lower strain energy than maintaining the half tube/helical tube (Figure 3C, labeled by “*”). Therefore, it is energetically preferred for a microrectangle to transform into the short tubes rather than a long tube or a helical tube (Figure 3C).

3.1.5. Wider Rectangles Perform Two-Phase Self-Folding, Narrower Rectangles Perform Single-Phase Self-Folding

Keeping the folding circumference C_f unchanged (by keeping layer thickness and swelling ratio unchanged) and the self-hindrance disabled, we next studied how the dimensions of microrectangle influence self-folding. The simulation was repeated with the width being changed in reference to C_f . The results indicated that all microrectangles self-folded into short tubes at the end. However, the number of phases, one or two, during self-folding is determined by the ratio between the folding circumference C_f and the width of postswelling rectangle w' (Figure 4A). If the width after swelling w' exceeds about 20% of C_f ($w'/C_f > 0.2$), the self-folding approached the shorter tube by first folding laterally (Figure 4A bottom row), which led to a long tube, and then twisting into a short tube. In contrast, if w' becomes less than 20% of C_f ($w'/C_f < 0.2$), the self-folding started with the longitudinal folding and directly transformed the microrectangle into the short tube (Figure 4A top row). Lateral folding, which produces a shorter tube, was shown to be energetically preferred for the folding rectangle regardless of the value of w'/C_f . In all the two phases self-folding cases, the secondary folding was bi-modal and could be either left-handed or right-handed.

3.1.6. Self-Hindrance Determines the End Point of Self-Folding

Collisions between different parts of the micropattern interrupt the above self-folding. To examine this effect, we repeated the above simulation with self-hindrance being enabled. In the simulation with self-hindrance, once mass-points collided with each other, the twisting in the secondary folding stopped, with

the helical angle stopping at ϕ . This angle was correlated to the ratio of width postswelling (w') to the folding circumference (C_f) (Figure 4B, also in Video S2 in the Supporting Information). For example, for the microrectangles that became half-tube in the primary folding ($w'/C_f = 0.5$), the helical angles were roughly 61.5° . When the width of the rectangle became wider (e.g., $w'/C_f = 1.0$), the self-hindrance took place earlier and caused a much smaller helical angle, leading to a straight tube ($\phi \approx 0^\circ$). In contrast, the microrectangle with a narrower width (e.g., $w'/C_f = 0.4$) was able to twist by a larger helical angle ($\phi \approx 77.7^\circ$) before being stopped by self-hindrance.

4. Experiments to Validate the Modeling Results

The above numerical model deciphered the complex dynamics behind self-folding of microrectangle. To verify the above modeling results, we conducted experiments by inkjet-printing 2D bilayered micropatterns made of hydrogels.

4.1. Verifying the Simulation Results

A high precision inkjet-printing platform was developed to deliver microdroplets of biomaterial-inks (about 160 pL per drop) onto a glass substrate, forming ink-spots of 140 μm diameter, where the droplets were assembled into predesigned micropatterns. Each micropattern consisted of two layers of distinct biomaterial-inks, with the biomaterial-ink of higher swelling rate (Gel-COOH-MA, 59%) forming the bottom layer and the biomaterial-ink of lower swelling rate (Gel-MA, 34%) forming the top layer. The thickness of each layer, which determined the curvature of self-folding, was controlled by the

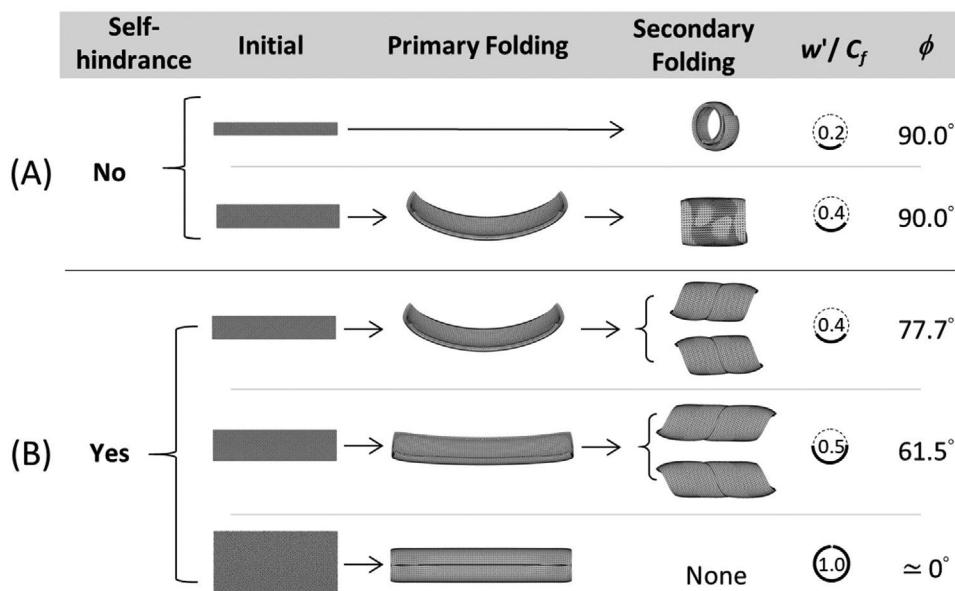


Figure 4. MSM modeling on bilayered microrectangle: the ratio between postswelling width (w') and folding circumference (C_f) determines the folding results: A) Without self-hindrance, all microrectangles fold into short tubes. The w'/C_f ratio determines the number of phases self-folding undergoes: one phase when $w'/C_f < 0.2$ (top row), two phases when $w'/C_f > 0.2$ (bottom row). B) With self-hindrance, the helical angle ϕ is a function of the w'/C_f ratio. Larger w'/C_f ratio results in a smaller helical angle.

number of ink-drops per inch. This arrangement enabled the micropatterns to fold away from the glass slide when being swollen by water. As-printed micropatterns were crosslinked in a photoinitiator contained organic solvent by an exposure to ultraviolet light (365 nm, 2 mW cm⁻², 5 min). Details of the inkjet printing are provided in the Supporting Information.

Having established the inkjet-printing platform, we proceeded to examine the accuracy of the mass-spring model on simulating the self-folding of bilayered microrectangles (Figure 5A,B). The biomaterial-inks were printed into microrectangles of 140 μm width and various layer thicknesses, which led to microtubes of various self-folding circumference C_f . Upon a rinse in phosphate buffer saline (PBS), these microrectangles were released from the glass slide and self-folded into microscopic tubes (Figure 5A). MSM that resembled

the inkjet-printed microrectangles was created and tested (Figure 5B). The results from simulation were consistent with the results from the inkjet-printed micropatterns. Both the experimental and simulated results showed the follows: 1) postswelling, if the width of microrectangle (w') was similar to the C_f of the microtube, the microtube approached a long and straight tube; 2) if w' was less than C_f , the microtube became a helical tube; 3) decreasing the w' -to- C_f ratio increased the helical angles ϕ ; and 4) when the micropattern was laterally symmetric, the microrectangles performed bi-modal, chiral twisting, which resulted in either right-handed or left-handed twisting (Figure 5A vs 5B).

4.2. Self-Folding of More Complex Micropatterns

Having validated the accuracy of the numerical model on predicting the self-folding of microrectangles, we continued to test on more complex micropatterns (Figure 5C,D and Figure 6) and found the experimental and simulated results fitting with each other. For example, a new micropattern consisting of 20 drop-spots was fabricated as shown in Figure 5C. The w' -to- C_f ratio of this micropattern (in which w' represented

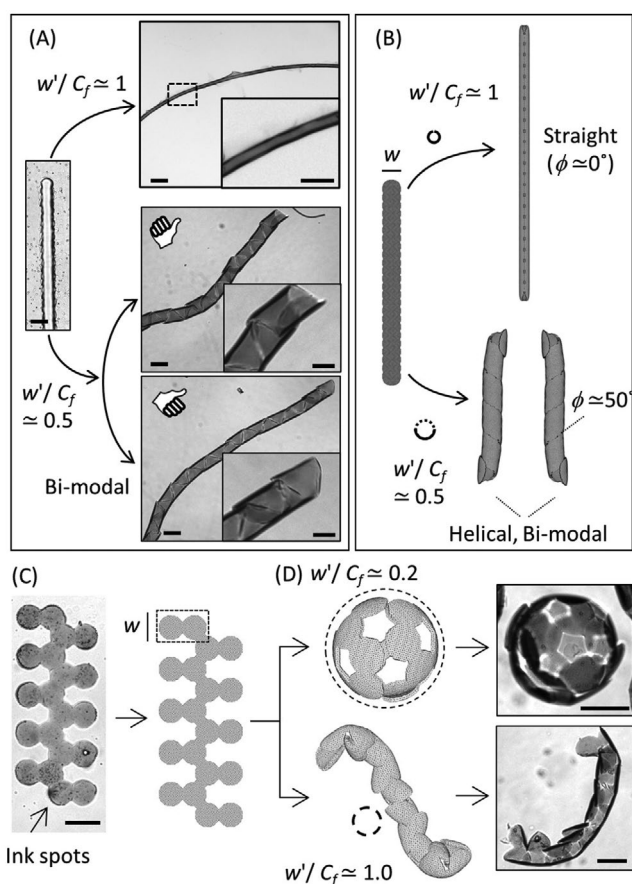


Figure 5. Validating simulation results with experiments. A,B) Self-folding of inkjet-printed microrectangles. A) The helical angle ϕ was correlated to the ratio between postswelling width (w') and folding circumference (C_f). $\phi \approx 0^\circ$ when $w'/C_f \approx 1$, leading to straight tubes (top). $\phi \approx 50^\circ$ when $w'/C_f \approx 0.5$, leading to helical tubes. The self-folding was bi-modal—the twisting of helical tubes was either right-handed (middle) or left-handed (bottom). B) This result validated the accuracy of the MSM model. C,D) Self-folding of a micropattern made of 20 drop-spots. The ratio of postswelling width (w') to folding circumference (C_f) determined the final 3D shape. The micropattern became a porous sphere when $w'/C_f \approx 0.2$ but a scorpion-like shape when $w'/C_f \approx 1$. Results from the modeling and experiments were consistent with each other. Scale bars for A,C,D) 200 μm, insets: 100 μm.

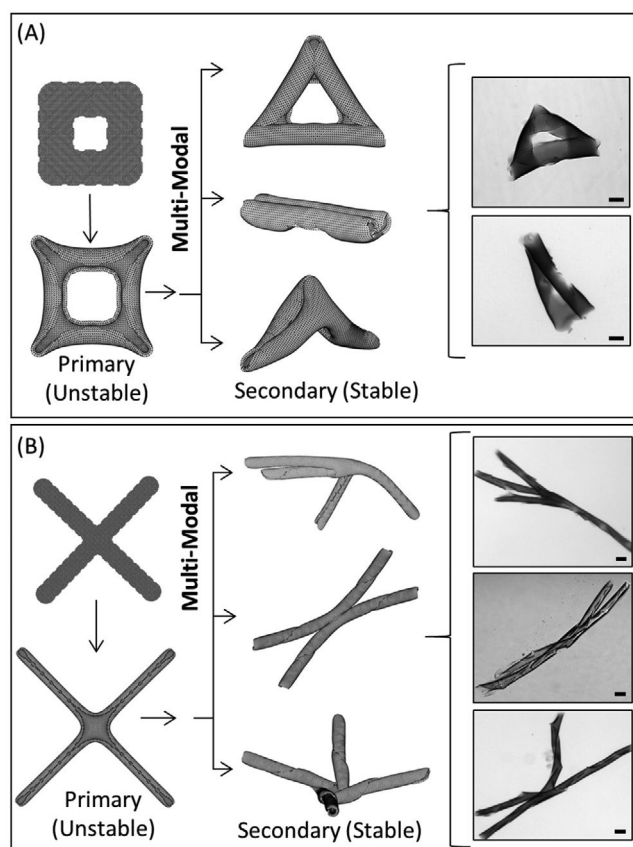


Figure 6. Self-folding of A) hollow square-like and B) cross-like micropatterns, in which $w'/C_f \approx 0.9$. The MSM model predicted the self-folding to be multi-modal and capable of generating three different 3D microstructures. Most of these microstructures were identified in the inkjet-printing experiments (right column). All scale bars: 100 μm

the postswelling width of drop-spot) was found capable of causing dramatic change to the final 3D microstructure. When the thicknesses of the two layers were adjusted to provide $\approx 0.2 w'/C_f$ ratio (Figure 5D, top), the direction of self-folding for each rectangle was longitudinal, and the micropattern self-folded into a porous sphere that resembles the isotropic tissue compartments, which are commonly seen in the lungs, cartilage, and fat tissues (also see Figure 1B). In contrast, when the thicknesses of the layers were decreased by fivefold, which increased the value of w'/C_f to 1, lateral folding became dominant and the micropattern self-folded into a “scorpion-like” 3D structure instead of the porous sphere (Figure 5D, bottom).

3D microstructures that were much more complex than microscopic tubes were formed when the ink-spots were organized into slightly more complex forms of micropatterns (Figure 6). These complex micropatterns were found to perform more unpredictable self-folding. For example, for a micropattern that resembled a hollow square (Figure 6A), the simulation predicted the micropattern to perform a multi-modal folding. Such folding included one primary folding and three distinct secondary foldings, leading to three different types of 3D microstructure. Two of these microstructures were identified from our inkjet-printed results (Figure 6A, right). Likewise, when the ink-spots were assembled into a cross-like pattern (Figure 6B), the simulation predicted three possible final 3D microstructures, and all three microstructures were observed from the inkjet-printed results (Figure 6B, right). The lack of experimental evidence for some of the simulated results might stem from a lower probability for certain imperfection (which determines the secondary phase of self-folding) to take place. For tissue-engineering applications, such multi-modal self-folding may be utilized as a tool to create scaffolds of more diverse morphology, such as the scaffold to regenerate a bone network. On the other hand, multi-modal self-folding may be considered as a pitfall to avoid, if identical 3D microstructures are desired.

4.3. Effects of External Forces and Boundary Conditions on Self-Folding

One unique advantage of the mass-spring model is the ease to apply arbitrary forces and boundary conditions, allowing the user to apply more realistic conditions to the simulated body. In the above studies, reactive forces that decelerated the folding motions were applied to the superficial mass-points to simulate drags by water. External forces may also come from other boundary conditions. For example, the self-folded 3D microstructure may be permanently bound to the substrate for a lab-on-chip application. Flows from the water surrounding the micropattern could also influence self-folding.

Using the numerical model, we found that the disturbance from the surrounding water can sometimes be necessary to achieve a desired self-folding. For example, we simulated the self-folding of a tubular network micropattern (Figure 7A). In this pattern, different regions had been assigned with different folding circumferences, which were C_{f1} for narrow rectangle region and C_{f2} for wider rectangle region ($C_{f1}: C_{f2} = 1:2$), respectively. In the absence of disturbance, the micropattern was

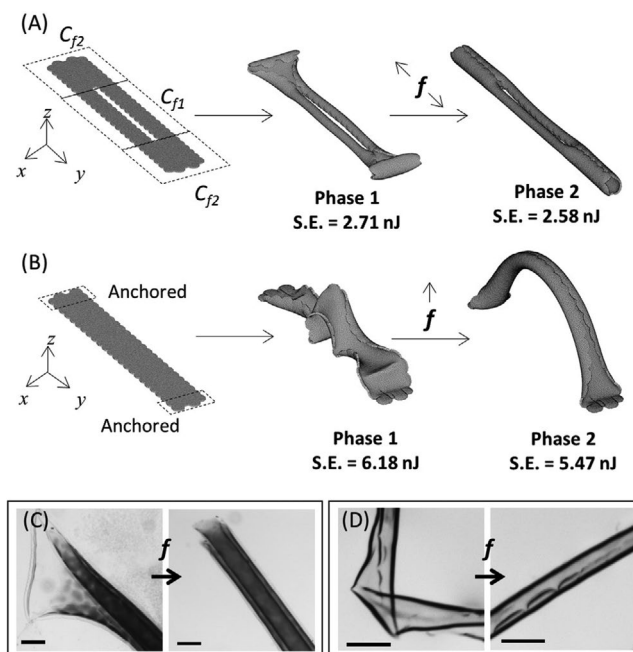


Figure 7. The MSM simulation showed that the self-folding of a complex micropattern might be trapped in an energy pitfall and yield an unwanted 3D shape. This energy pitfall, fortunately, can be overcome by applying external forces to force the 3D microstructure to refold and transform into a different 3D shape. This figure shows two examples. A) A branched micropattern with folding circumferences C_{f1} for the center region and C_{f2} for the ends ($C_{f1}: C_{f2} = 1:2$) performed unwanted-folding at the ends, which trapped the self-folding at a strain energy (S.E.) pitfall of 2.71 nJ (Phase 1). This unwanted folding can be rescued by applying an external force “ f ” in the longitudinal direction (along y -direction), which refolds the side tubes and transform the side tubes, into new structures of 2.58 nJ energy state (Phase 2). B) Similar effects happened on a microtubular bridge with two ends anchored on the substrate. Simulation results showed that the micropattern could be wrinkled and trapped at an energy pitfall (6.18 nJ) without further deformation. Applying an agitation (“ f ” along z -direction) may force the wrinkled structure to transform into the bridge-like microtube (S.E. = 5.74 nJ). These effects have been found in our experimental models as shown in (C,D), in which unwanted self-folding was corrected by refolding the micropattern using external forces. All scale bars: 200 μm .

predicted to self-fold into the 3D microstructure with unwanted, nontubular ends (Figure 7A, Phase 1). This state was found energetically stable, which means the self-folding had been trapped in an energy pitfall with strain energy of 2.71 nJ, and the microstructure would not perform further deformation. Fortunately, flow from the surrounding water (external force “ f ” along y -direction in Figure 7A) may overcome this energy pitfall and force this 3D structure to refold into a branched microtube (with lower strain energy of 2.58 nJ comparing to phase 1 folding) that mimics an interface between arterial and venous capillary vessels (Figure 7A, Phase 2). In our experiments, such a folding pitfall was observed and could be fixed by pipetting water next to the structure (Figure 7C). Likewise, a microrectangle anchored to the substrate on the two ends can easily become wrinkled (Figure 7B, Phase 1) and trapped at this energy pitfall (with strain energy of 6.18 nJ) without further

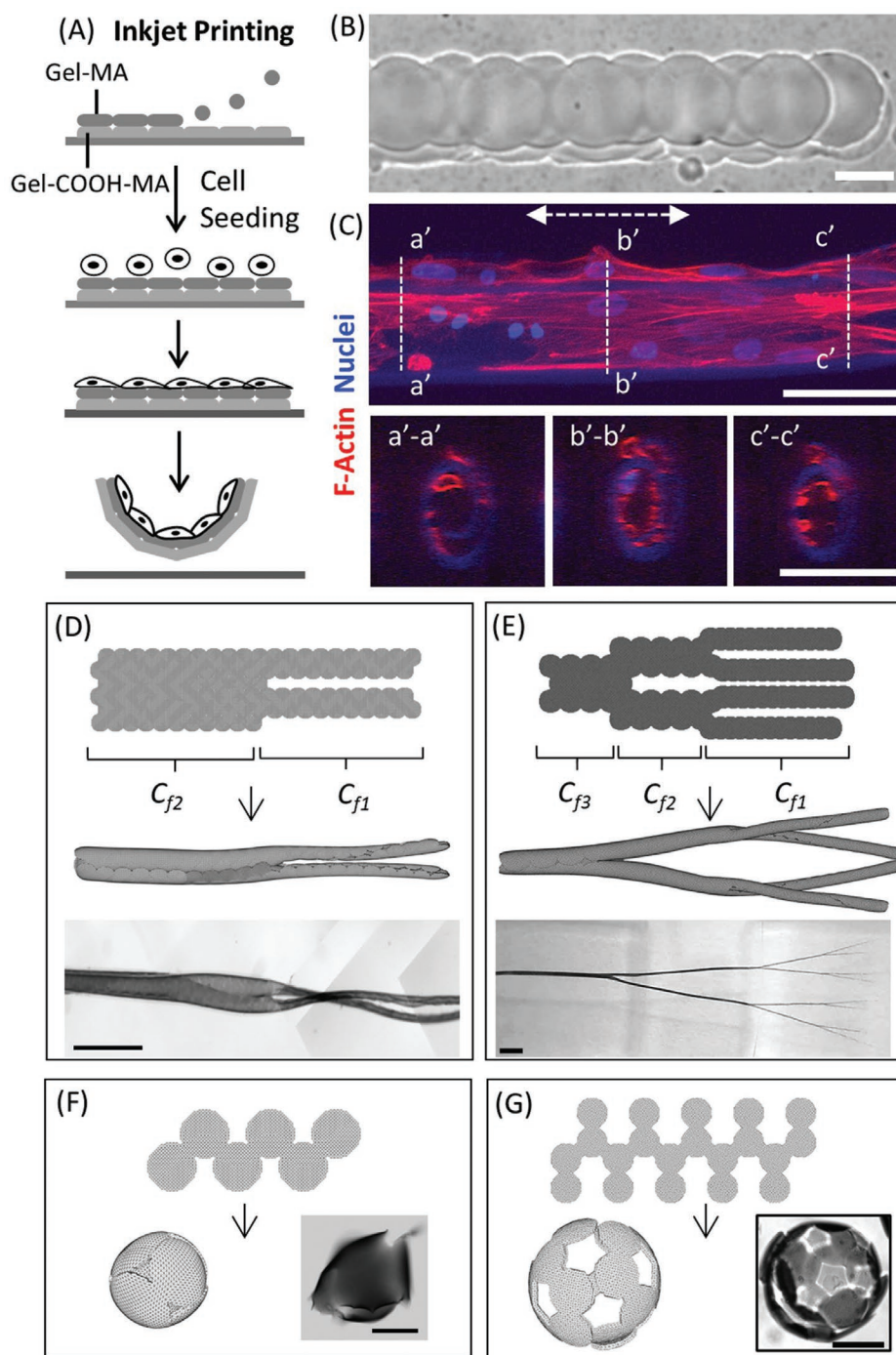


Figure 8. A) Schematic of cell seeding and micropattern self-folding. Cells are seeded on the inkjet-printed bilayer micropatterns for a day, and micropatterns with cells are released from the substrate for self-folding. B, C) Encapsulating human mesenchymal stem cells in self-folding microtubes. B) The MSCs were seeded on the microrectangles, which was released from the substrate 1 day after 2D cell culture. C) After being cultured in 3D for 3 days, MSCs in the microtube became uniformly distributed along the tube, with cell nuclei and cytoskeleton (F-actin) self-aligned by the direction of the microtube. D–G) Self-folding micropatterns forming biomimetic microstructures were designed by the MSM algorithm and fabricated by inkjet-printing. D) These biomimetic microstructures include branched tubes, E) hierarchical branched tubes, F) spheres, and G) porous spheres. Scale bars: B) 100 μm ; C) 50 μm ; D) 500 μm ; E) 1 mm; F, G) 200 μm .

deformation. An agitation from the surrounding fluid (external force “ f ” along z -direction in Figure 7B), which forced the entangled structure to refold, may rescue the microstructures from

wrinkling and transform the microstructures into a bridging microtube with strain energy of 5.47 nJ as desired. Such a phenomenon was also observed in our experiments (Figure 7D).

5. Applying MSM to Designing Self-Folding Microstructures for Tissue Engineering Application

Tissues in our body consist of various kinds of 3D microstructures. The above self-folding approach can be applied to assembling organic compounds suitable for tissue engineering into these 3D microstructures. As a proof of concept, human mesenchymal stem cells (MSC) were seeded onto the gelatin-based, microrectangles of 1.2 w' -to- C_f ratio on a glass slide (Figure 8B) and incubated in standard MSC culture media, under 37 °C and 5% CO₂. One day after cell seeding, the microrectangles were detached from the glass slide using PBS and allowed to self-fold into microscopic tubes. By 4 days post cell-seeding (which were 3 days after self-folding), MSCs became uniformly distributed along the tube, with cell nuclei and F-actin self-aligned by the direction of the microtube, as shown by confocal microscope images (Figure 8C). Analyzing the confocal images by cross-sections of the tube (Figure 8C, a'-a', b'-b', and c'-c') showed that the tube with embedded MSCs had a 30–50 μm inner diameter, which was comparable with the typical size of MSC (15–30 μm).^[26] Without self-folding, populating such a microtubular scaffold with cells is often difficult, as cells can easily block the microstructures as reported elsewhere.^[7c,27] Experimental details about biomaterial preparation (synthesis of Gel-MA and Gel-COOH-MA), printing procedures (printing, crosslinking, and self-folding), and cell seeding, culturing and staining are provided in the Supporting Information. Since MSCs were capable of differentiating into the phenotypes of cells in muscles and tendons,^[28] microtubes as such are promising building blocks to regenerate muscles and tendons. These building blocks are also promising for housing other types of cells and regenerating other kinds of linear tissues, including microvessels, nerve bundles, and lymphatic conduits.

Besides microtubular structures, the human body contains more complex 3D microstructures, including branched tubes, hollow spheres, and interconnected pores. We applied the numerical model to designing the 2D micropatterns that could self-fold into these biomimetic microstructures, followed by using the inkjet printer to fabricate these micropatterns. The inkjet-printed micropatterns performed expected self-folding. To make the self-folding of these micropatterns more repeatable and predictable, the micropatterns were printed such that different zones of the micropatterns had a w' -to- C_f ratio that was either close to 1 (which locally produce a straight tube-like structure) or less than 0.2 (which had negligible self-twisting). This minimized the effect of multi-modal folding, as previously explained in Figure 4. By combining two types of microrectangles that had distinct length, width, and folding circumference C_f , the inkjet-printing created branched microtubes that resembled a branched nerve or microvessel (Figure 8D). Combining more than two types of microrectangles, as shown in Figure 8E (also in Video S5, Supporting Information), led to a tree of microtubes with a hierarchical and branched structure. Such a branched structure may support the regeneration of a network of microvessels or nerves.

The above simulation-based design and the inkjet-printing based microfabrication were also used to produce spherical

microstructures. These structures resemble the shapes of porous, random, and isotropic tissues that can be found in cartilages, bones, and fats. For example, microspherical structures were fabricated by printing the ink-spots into micropatterns that resembled an unfolded hollow polyhedron, such as unfolded hexahedron and unfolded icosahedron (Figure 8F,G).

6. Conclusion

Still in its infancy, the technology of self-folding microstructures is particularly promising for creating biomimetic microstructure as scaffolds for tissue regeneration. The development of this technology, however, requires more fundamental understanding of how heterogeneous volume change determines the shape-transformation of the deforming body. Here we helped bridge this knowledge gap by creating the above MSM algorithm, which is mathematically simple and yet flexible for simulating highly complex microstructures. By simulating the deformation of the self-folding body in real-time, we learned that the shape transformation of the self-folding body is a two-phase procedure. In the primary phase, the self-folding body releases the majority of strain energy and performs mostly predictable deformation. In the secondary phase, the self-folding undergoes fine-tuning, such as twisting, which may significantly change the overall shape. Most interestingly, the secondary phase of self-folding may undergo multi-modal shape-transformation, which transforms identical folding bodies into dramatically different 3D shapes. Finally, the self-hindrance of the self-folding body interrupts deformation and determines the final shape of the self-folding body.

To validate the modeling results, we conducted experiments by using photo-crosslinkable polymers of distinct water-swelling rates. A high-precision inkjet printer was used to pattern the polymers into bilayered micropatterns that resembled the shapes of the numerical models. A simple cell study using human MSC was conducted as a proof of concept. These micropatterns performed self-folding in water, leading to tubular, spherical, and more complicated structures that resemble the topography of living tissues, such as branched tubes. Multi-modal self-folding was observed in experiments, which verified the prediction by the numerical models. We expect that the above knowledge, the MSM-based model, and the inkjet-printing platform to greatly contribute to the research on self-folding microstructures, as well as applications to regenerative medicine.

7. Experimental Section

Detailed explanation on the mass-spring model, the MATLAB-based coding for the model, and experiments are provided in the Supporting Information.

Supporting Information

Supporting Information is available from the Wiley Online Library or from the author.

Acknowledgements

The authors would like to thank the National Science Foundation (CBET-1605604) and the Drexel University for funding supports.

Conflict of Interest

The authors declare no conflict of interest.

Keywords

inkjet printing, mass-spring method modeling, microstructures, self-folding structures, tissue engineering

Received: May 6, 2020

Revised: June 6, 2020

Published online: August 12, 2020

- [1] a) M. C. Phipps, W. C. Clem, J. M. Grunda, G. A. Clines, S. L. Bellis, *Biomaterials* **2012**, *33*, 524; b) S. V. Murphy, A. Atala, *Nat. Biotechnol.* **2014**, *32*, 773; c) R. Gauvin, Y.-C. Chen, J. W. Lee, P. Soman, P. Zorlutuna, J. W. Nichol, H. Bae, S. Chen, A. Khademhosseini, *Biomaterials* **2012**, *33*, 3824; d) R. Zhang, N. B. Larsen, *Lab Chip* **2017**, *17*, 4273; e) J. S. Miller, K. R. Stevens, M. T. Yang, B. M. Baker, D.-H. T. Nguyen, D. M. Cohen, E. Toro, A. A. Chen, P. A. Galie, X. Yu, *Nat. Mater.* **2012**, *11*, 768; f) L. Shor, S. Güçeri, R. Chang, J. Gordon, Q. Kang, L. Hartsock, Y. An, W. Sun, *Biofabrication* **2009**, *1*, 015003.
- [2] a) M. Wang, C. Cui, M. M. Ibrahim, B. Han, Q. Li, M. Pacifici, J. T. R. Lawrence, L. Han, L. H. Han, *Adv. Funct. Mater.* **2019**, *29*, 1808967; b) R. D. Cardwell, L. A. Dahlgren, A. S. Goldstein, *J. Tissue Eng. Regen. Med.* **2014**, *8*, 937; c) A. J. Engler, S. Sen, H. L. Sweeney, D. E. Discher, *Cell* **2006**, *126*, 677; d) R. McBeath, D. M. Pirone, C. M. Nelson, K. Bhadriraju, C. S. Chen, *Dev. Cell* **2004**, *6*, 483; e) V. Vogel, M. Sheetz, *Nat. Rev. Mol. Cell Biol.* **2006**, *7*, 265.
- [3] a) J. D. Humphrey, E. R. Dufresne, M. A. Schwartz, *Nat. Rev. Mol. Cell Biol.* **2014**, *15*, 802; b) J. K. Mouw, G. Ou, V. M. Weaver, *Nat. Rev. Mol. Cell Biol.* **2014**, *15*, 771.
- [4] a) G. R. Ragety, D. J. Griffon, H.-B. Lee, L. P. Fredericks, W. Gordon-Evans, Y. S. Chung, *Acta Biomater.* **2010**, *6*, 1430; b) M. J. Moore, J. A. Friedman, E. B. Lewellyn, S. M. Mantila, A. J. Krych, S. Ameenuddin, A. M. Knight, L. Lu, B. L. Currier, R. J. Spinner, R. W. Marsh, A. J. Windebank, M. J. Yaszemski, *Biomaterials* **2006**, *27*, 419.
- [5] M. J. Madou, *Fundamentals of Microfabrication: The Science of Miniaturization*, CRC Press, Boca Raton, FL **2002**.
- [6] a) S. You, J. Li, W. Zhu, C. Yu, D. Mei, S. Chen, *J. Mater. Chem. B* **2018**, *6*, 2187; b) W. Zhu, K. R. Tringale, S. A. Woller, S. You, S. Johnson, H. Shen, J. Schimelman, M. Whitney, J. Steinauer, W. Xu, T. L. Yaksh, Q. T. Nguyen, S. Chen, *Mater. Today* **2018**, *21*, 951.
- [7] a) B. Zhang, M. Montgomery, M. D. Chamberlain, S. Ogawa, A. Korolj, A. Pahnke, L. A. Wells, S. Massé, J. Kim, L. Reis, *Nat. Mater.* **2016**, *15*, 669; b) D. B. Kolesky, K. A. Homan, M. A. Skylar-Scott, J. A. Lewis, *Proc. Natl. Acad. Sci. USA* **2016**, *113*, 3179; c) R. M. Linville, N. F. Boland, G. Covarrubias, G. M. Price, J. Tien, *Cell Mol. Bioeng.* **2016**, *9*, 73; d) C. M. Murphy, M. G. Haugh, F. J. O'Brien, *Biomaterials* **2010**, *31*, 461.
- [8] P. Thevenot, A. Nair, J. Dey, J. Yang, L. Tang, *Tissue Eng., Part C* **2008**, *14*, 319.
- [9] S. V. Murphy, A. Atala, *Nat. Biotechnol.* **2014**, *32*, 773.
- [10] J. Hammer, L.-H. Han, X. Tong, F. Yang, *Tissue Eng., Part C* **2014**, *20*, 169.
- [11] a) A. Azam, K. E. Laflin, M. Jamal, R. Fernandes, D. H. Gracias, *Biomed. Microdevices* **2011**, *13*, 51; b) G. Stoychev, N. Pureskiy, L. Ionov, *Soft Matter* **2011**, *7*, 3277; c) A. S. Gladman, E. A. Matsumoto, R. G. Nuzzo, L. Mahadevan, J. A. Lewis, *Nat. Mater.* **2016**, *15*, 413; d) K. Kuribayashi-Shigetomi, H. Onoe, S. Takeuchi, *PLoS One* **2012**, *7*, e51085.
- [12] a) V. Stroganov, S. Zakharchenko, E. Sperling, A. K. Meyer, O. G. Schmidt, L. Ionov, *Adv. Funct. Mater.* **2014**, *24*, 4357; b) Q. He, T. Okajima, H. Onoe, A. Subagyo, K. Sueoka, K. Kuribayashi-Shigetomi, *Sci. Rep.* **2018**, *8*, 4556; c) L. Vannozzi, I. C. Yasa, H. Ceylan, A. Mencias, L. Ricotti, M. Sitti, *Macromol. Biosci.* **2018**, *18*, 1700377.
- [13] a) T. F. Teshima, H. Nakashima, Y. Ueno, S. Sasaki, C. S. Henderson, S. Tsukada, *Sci. Rep.* **2017**, *7*, 17376; b) M. Jamal, S. S. Kadam, R. Xiao, F. Jivan, T. M. Onn, R. Fernandes, T. D. Nguyen, D. H. Gracias, *Adv. Healthcare Mater.* **2013**, *2*, 1142.
- [14] a) M. Nadgorny, Z. Xiao, C. Chen, L. A. Connal, *ACS Appl. Mater. Interfaces* **2016**, *8*, 28946; b) G. Huang, Y. Mei, D. J. Thurmer, E. Coric, O. G. Schmidt, *Lab Chip* **2009**, *9*, 263.
- [15] S. Timoshenko, *J. Opt. Soc. Am.* **1925**, *11*, 233.
- [16] X. Yu, L. Zhang, N. Hu, H. Grover, S. Huang, D. Wang, Z. Chen, *Appl. Phys. Lett.* **2017**, *110*, 091901.
- [17] O. Stephansson, *Philos. Trans. R. Soc. London A* **1976**, *283*, 153.
- [18] a) A. J. C. Ladd, J. H. Kinney, *Phys. A* **1997**, *240*, 349; b) M. Kot, H. Nagahashi, P. Szymczak, *Visual Comput.* **2014**, *31*, 1339; c) M. Kot, H. Nagahashi, P. Szymczak, *Visual Comput.* **2015**, *31*, 1339.
- [19] G. Béda, *Int. Appl. Mech.* **2003**, *39*, 123.
- [20] a) K. Miller, G. Joldes, D. Lance, A. Wittek, *Commun. Numer. Methods Eng.* **2007**, *23*, 121; b) Z. A. Taylor, M. Cheng, S. Ourselin, *Int. Conf. Med. Image Comput. Comput. Assisted Intervention* **2007**, *4791*, 701; c) O. Comas, Z. A. Taylor, J. Allard, S. Ourselin, S. Cotin, J. Passenger, *Int. Symp. Biomed. Simul.* **2008**, *5104*, 28.
- [21] M. Xia, H. Zhou, Q. Li, H. Chen, Y. Wang, S. Wang, *Bull. Seismol. Soc. Am.* **2017**, *107*, 2194.
- [22] S. S. Rao, *Mechanical Vibration*, Pearson, ON, New York **2016**.
- [23] G. N. Greaves, *Notes Rec. R. Soc.* **2013**, *67*, 37.
- [24] R. Soutas-Little, *Engineering Mechanics: Statics*, Pearson, NJ **2010**.
- [25] B. R. Munson, W. W. Huebsch, A. P. Rothmayer, *Fundamentals of Fluid Mechanics*, Wiley, New York **2012**.
- [26] a) T. E. Krueger, D. L. Thorek, S. R. Denmeade, J. T. Isaacs, W. N. Brennen, *Stem Cells Transl. Med.* **2018**, *7*, 651; b) L. Liu, L. Tseng, Q. Ye, Y. L. Wu, D. J. Bain, C. Ho, *Sci. Rep.* **2016**, *6*, 26271.
- [27] M. A. Traore, S. C. George, *Tissue Eng., Part B* **2017**, *23*, 505.
- [28] a) J. G. Barber, A. M. Handorf, T. J. Allee, W. J. Li, *Tissue Eng. Part A* **2013**, *19*, 1265; b) T. W. Qin, Y. L. Sun, A. R. Thoreson, S. P. Steinmann, P. C. Amadio, K. N. An, C. Zhao, *Biomaterials* **2015**, *51*, 43; c) J. Liu, H. H. Xu, H. Zhou, M. D. Weir, Q. Chen, C. A. Trotman, *Acta Biomater.* **2013**, *9*, 4688.